



Controlling the mechanical behavior of dual-material 3D printed meta-materials for patient-specific tissue-mimicking phantoms

Kan Wang^{a,b,*}, Yuanshuo Zhao^a, Yung-Hang Chang^{a,b}, Zhen Qian^d, Chuck Zhang^{a,b}, Ben Wang^{a,b,c}, Mani A. Vannan^d, Mao-Jiun Wang^e

^a H. Milton Stewart School of Industrial and Systems Engineering, Georgia Institute of Technology, Atlanta, GA 30332, USA

^b Georgia Tech Manufacturing Institute, Georgia Institute of Technology, Atlanta, GA 30332, USA

^c School of Materials Science and Engineering, Georgia Institute of Technology, Atlanta, GA 30332, USA

^d Department of Cardiovascular Imaging, Piedmont Heart Institute, 95 Collier Road, Atlanta, GA 30309, USA

^e Department of Industrial Engineering and Engineering Management, National Tsing-Hua University, Hsinchu, Taiwan

ARTICLE INFO

Article history:

Received 14 August 2015

Received in revised form 30 October 2015

Accepted 5 November 2015

Available online 7 November 2015

Keywords:

Multi-material 3D printing

Tissue-mimicking phantoms

Meta-materials

Nonlinear mechanical properties

Strain-stiffening behavior

ABSTRACT

Patient-specific tissue-mimicking phantoms are becoming available with the advent of additive manufacturing. Phantoms currently in use are focused on the geometrical accuracy and mechanical properties under small deformation. Mimicking the mechanical properties at large deformation is challenging because of the inherent difference between the mechanical behaviors of polymeric materials and that of human tissues. In this study, the mechanical behavior of soft tissues under a uniaxial tension is mimicked by dual-material 3D printed meta-materials with stiff micro-structured fibers embedded in a soft polymeric matrix. Although the two base materials are strain-softening polymers, some of the designed meta-materials demonstrate certain degree of strain-stiffening behavior. Further investigation shows how the stress-strain curve of the meta-materials can be controlled by the design parameters. Sensitivity analysis is used to study the effects of each parameter. General design guidelines are proposed based on the results of the experiments. Dual-material 3D printed meta-materials have great potential in fabricating patient-specific phantoms with accurate mechanical properties that are associated with the gender, age, ethnicity, and other physiological/pathological characteristics. Mechanically accurate phantoms can play an important role in a variety of biomedical applications, including validation of computational models, testing of medical devices, surgery planning, medical education and training, and doctor-patient interaction.

Published by Elsevier Ltd.

1. Introduction

Given the difficulties in procuring real human tissue samples, tissue-mimicking phantoms are invaluable to experimental biomedical research. The most common applications include the development and validation of medical imaging modalities, such as ultrasound [1,2], computed tomography (CT) [3], magnetic resonance imaging (MRI) [4,5,6,7], and others [8]. Simulation of electromagnetic properties of tissues [9], mimicking mechanical properties [10], and focused ultrasound ablation [11] are additional ways that tissue-mimicking phantoms are used. Most of these applications are for generalized studies and are not patient-specific. Instead, idealized phantoms that use population averages are used. Individual differences among patients are usually overlooked. In individual cases, the information that the population-averaged phantoms can provide is very limited since specific information for each patient, such as age, sex, race and medical history, may heavily affect the tissue properties [12,13,14].

Recent advances in three dimensional (3D) printing technologies use computational models of an individual patient's CT or MRI scan to reconstruct phantoms that mimic the patient's tissue [15]. Patient-specific phantoms contain individual information and they have great potential in many biomedical applications and clinical benefits such as computational model validation, medical device testing, surgery planning, medical education, and doctor-patient interaction.

3D printing has already been used in various biomedical applications including prosthetics [16], orthopedic implants [17,18,19], and tissue/organ printing [20,21,22]. As an emerging biomedical approach, patient-specific tissue-mimicking phantoms aim to represent an accurate anatomic structure specific for each case. 3D printing technologies are perfectly suited for this purpose since they feature high customizability, high geometrical complexity, and high cost effectiveness at a low production volume. More advanced applications of patient-specific tissue-mimicking phantoms go further than anatomic accuracy. This is particularly true for the phantoms that aim to mimic soft tissues, a primary group of tissue which binds, supports and protects our human body and structures, such as tendons, ligaments, blood vessels, and skins. For example, the study of aorta valves in

* Corresponding author at: 813 Ferst Drive, RM 222, Atlanta, GA 30332, USA.
E-mail address: kan.wang@gatech.edu (K. Wang).

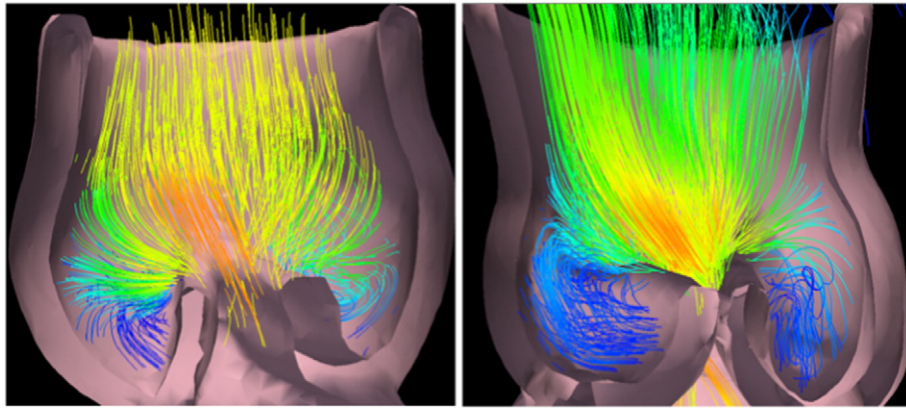


Fig. 1. Streamline visualizations of the simulated blood flow in a (a) healthy and a (b) stenotic aortic root.

dynamics involves the investigation of the interactions between the blood stream and the leaflets structure [23,24]. Current computational modeling for this problem usually employs a quasi-static approach in which rigid boundary is assumed for any given moment and the structural analysis and the flow simulations are conducted separately [25, 26], as shown in Fig. 1. As the quasi-static models are simplifications of the more complex full dynamic solid–fluid coupling problem, the effectiveness of those models needs to be validated with physical experiments using aorta root phantoms. Phantoms used in this type of study need to mimic, not only the anatomic structure, but also the mechanical properties of the real aorta tissue. This offers a new challenge to 3D printed phantoms since the printable materials are limited. Biglino et al. demonstrated the fabrication of compliant arterial phantoms with Polyjet technology that deposits liquid photopolymer layer by layer through orifice jetting and then solidifies by UV exposure [27]. They reported that TangoPlus, a rubber-like material used by StratasysConnex series 3D printers, has similar mechanical properties compared to real tissue. Cloonan et al. did a comparative study on commonly used tissue-mimicking materials and 3D printable materials, including TangoPlus, using the abdominal aortic aneurysm phantoms as the target application [15]. The results suggested that the performance of TangoPlus is better than the more commonly used poly (dimethylsiloxane) (PDMS) Sylgard elastomers in terms of uniaxial tensile properties.

Although phantom materials such as TangoPlus can mimic soft tissues at a small strain range (<3%), their practicality in biomedical

applications are limited since the working strain range of soft tissues are usually much larger. For example, because of the substantial blood pressure change within each cardiac cycle, human aortic root tissues typically undergo large deformations (>10%) in vivo [28,29]. The stress–strain curves of the polymeric materials and the biomaterials are inherently different in such a large strain range. Specifically, the soft tissues typically exhibit a strain-stiffening behavior in their working strain range, whereas the polymeric materials are initially strain-softening due to the primary creep. Fig. 2 outlines the typical stress–strain curves of a soft biological tissue and a polymeric material, assuming they have similar mechanical properties at a small strain range. As the plot suggests, the polymer material and soft tissue have very different mechanical behaviors at higher strain levels. Such difference prevents the use of polymeric phantoms in many biomedical studies that employ simulated working environment of soft tissues. For example, current 3D printed aorta models cannot be used for the pre-operative assessment of the transcatheter aortic valve replacement (TAVR). TAVR is a less invasive treatment option for severe aorta stenosis (AS) patients who are at high surgical risk. In order to achieve optimal clinical outcomes, an individualized assessment of the interactions between the native aortic tissue, the prosthesis and the blood flow is critical. The peak strain of human aortic tissues is typically larger than 10%, where the mechanical responses of the aortic tissue and the TangoPlus differ significantly.

In order to mimic the convex stress–strain curve of soft tissue, dual-material 3D printed meta-materials with micro-structured reinforcement embedded in a soft polymeric matrix were developed [30]. Strain-stiffening behaviors at certain degree were observed in two of those basic patterns. In this study, the effects of each design parameter of the two basic designs on the mechanical properties were investigated. A guideline of controlling the mechanical properties, including the initial modulus, maximum modulus, and the strain at inflection point, of the dual-material 3D printed meta-materials were summarized.

2. Materials and methods

2.1. The mechanism of strain-stiffening

The strain-stiffening behavior of soft tissues comes from the interaction between elastin and collagen [31]. Soft tissues in the human body work like fiber reinforced composite structures, where elastin and proteoglycans are the matrix and collagen fibrils are the reinforcements. Elastin is a protein that forms the major constituent of the extracellular matrix of soft tissues. It is usually in the form of thin strands that are long and flexible. Elastin molecules build up a 3D rubber-like network, which may be stretched to about 250% of the unloaded length. Its mechanical behavior is essentially linear elastic with marginal relaxation effects [32]. Collagen is a macromolecular protein with a length of

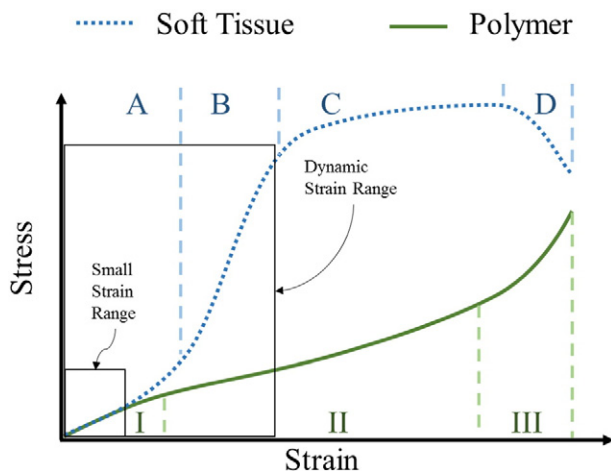


Fig. 2. Comparison of the mechanical behaviors of soft tissue and polymer. (a) Typical stress–strain curves of a soft tissue (dotted line) and a polymer (solid line). Soft tissue: A – toe region, B – elastic region, C – plastic region, D – failure region. Polymer: I – primary creep, II – secondary creep, III – tertiary creep.

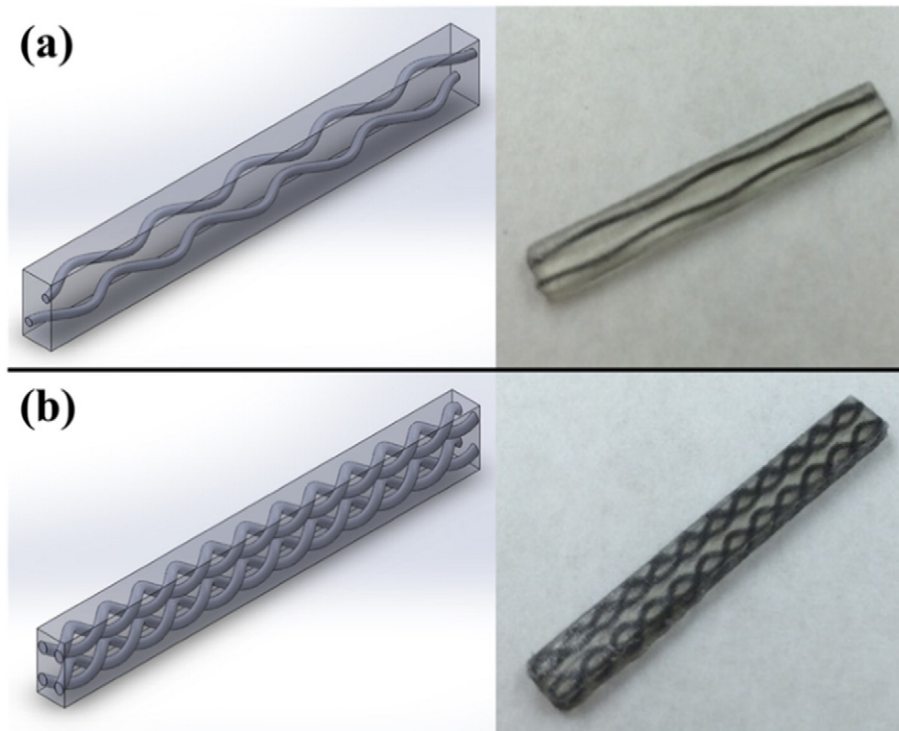


Fig. 3. CAD models and printed samples of three meta-materials: (a) sinusoidal wave design, (b) double helix design.

about 280 nm. Collagen molecules are linked to each other by strong covalent bonds to form collagen fibrils that are much stiffer than the elastin. Depending on the primary function of the tissue and its requirement of strength, the diameter of collagen fibrils varies around 1.5 μm [33]. The strain-stiffening effect can be explained by the self-aligning and straightening of collagen fibrils [34,35,36]. Initially, collagen fibrils are randomly oriented, wavy, and in a relaxed condition when the deformation is small. Since the elastin is mainly responsible for load carrying at this stage, the stress–strain relation is approximately linear and the modulus is close to that of elastin (0.1–2 MPa). As the deformation increases, collagen fibers start to align with the direction of tension and carry loads. The wavy collagen fibers gradually elongate and this results in an increasing modulus, hence the convex stress–strain curve. After collagen fibers are entirely straightened along the load direction, the modulus of soft tissue reaches its maximum and the stress–strain curve becomes almost linear again with a slight concave that is caused by relaxation.

Inspired by this stretching mechanism of soft tissues, we decided to use the dual-materials meta-material structures to mimic the mechanical behavior of soft tissues. Even though it is impossible to print

nanoscale fibrils, we imitated the self-aligning and straightening process of stiff fibers at a larger scale by embedding wavy, stiff microstructures into soft polymeric matrix. Theoretically, the stiff structures would straighten up during elongation and compensate for the creep of the matrix polymer, or even outweigh the effect of creep, resulting in an increasing slope on the stress–strain curve. Indeed, strain-stiffening behaviors at certain degree were observed in two of the designed patterns, sinusoidal wave (SW) and double helix (DH) [30]. The computer-aided design (CAD) model (SOLIDWORKS 2015 SP4.0) and 3D printed samples of the two designs are demonstrated in Fig. 3.

The two pattern each have three design parameters that can affect the mechanical properties. The design parameters for the SW design are the wavelength, λ ; the amplitude, A , of the sinusoidal wave; and the radius of fibers, r_f . The design parameters for the DH design are the radius of the helix, r_H ; the pitch, h ; and the radius of fibers, r_f . The design parameters provide an opportunity to tune the mechanical properties of the meta-materials to match those of the target soft tissue. In order to investigate the effect of each parameter, a series of parameter-wise variants were designed and tested.

Table 1
Parameter settings of the 12 variants of the SW design.

	Variant code	Wavelength, λ (mm)	Amplitude, A (mm)	Radius of fiber, r_f (mm)
λ -variants	Default SW_W5A06R03	5	0.6	0.3
	SW_W1A06R03	1	0.6	0.3
	SW_W3A06R03	3	0.6	0.3
	SW_W7A06R03	7	0.6	0.3
	SW_W9A06R03	9	0.6	0.3
A -variants	SW_W5A00R03	5	0 (straight)	0.3
	SW_W5A02R03	5	0.2	0.3
	SW_W5A04R03	5	0.4	0.3
	SW_W5A06R01	5	0.6	0.1
	SW_W5A06R02	5	0.6	0.2
r_f -variants	SW_W5A06R04	5	0.6	0.4
	SW_W5A06R05	5	0.6	0.5

Table 2
Parameter settings of the 11 variants of the DH design.

	Variant code	Pitch, h (mm)	Radius of helix, r_H (mm)	Radius of fiber, r_f (mm)
h -variants	Default DH_P5H06R02	5	0.6	0.2
	DH_P1H06R02	1	0.6	0.2
	DH_P3H06R02	3	0.6	0.2
	DH_P7H06R02	7	0.6	0.2
	DH_P9H06R02	9	0.6	0.2
r_H -variants	DH_P5H04R02	5	0.4	0.2
	DH_P5H05R02	5	0.5	0.2
	DH_P5H07R02	5	0.7	0.2
	DH_P5H08R02	5	0.8	0.2
	DH_P5H06R01	5	0.6	0.1
r_f -variants	DH_P5H06R03	5	0.6	0.3

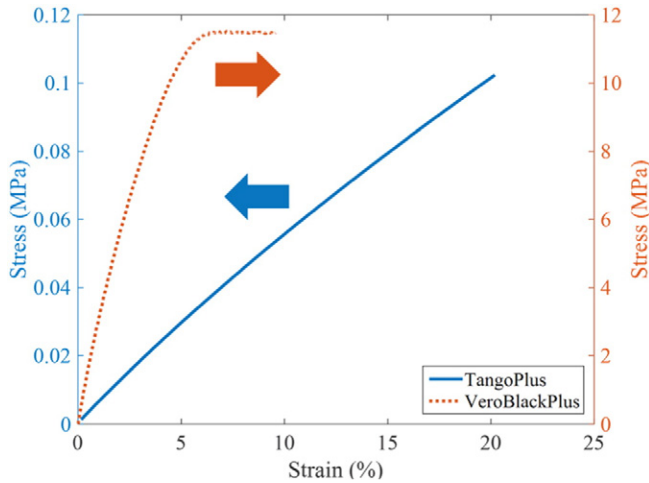


Fig. 4. Stress–strain curves of pure TangoPlus sample (solid, left y-axis) and VeroBlackPlus sample (dotted, right y-axis).

2.2. Design of meta-material samples

A default parameter setting was defined for each design. To investigate the effect of a single parameter, variants were designed with different values of the particular parameter, while other parameters were kept at their default values. The scope of this work was limited to studying the effect of a single parameter because simultaneously changing two or more parameters may generate geometrical conflicts with the current designs. It should be noted that the effects of interactions between two or more parameters may also exist. The parameter settings of the variants are summarized in the following sections. Three samples were fabricated and tested for each variant.

2.2.1. Variants of the sinusoidal wave design

The sinusoidal curve pattern is commonly used as an assumption for theoretical analysis or numerical simulation of natural wavy fibrous systems. The default parameter setting of the SW design is $\lambda = 5$ mm, $A = 0.6$ mm, and $r_f = 0.3$ mm. Other than the default level, variants with 4 levels of λ , 3 levels of A , and 4 levels of r_f were designed. Table 1 summarizes the total of 12 variants.

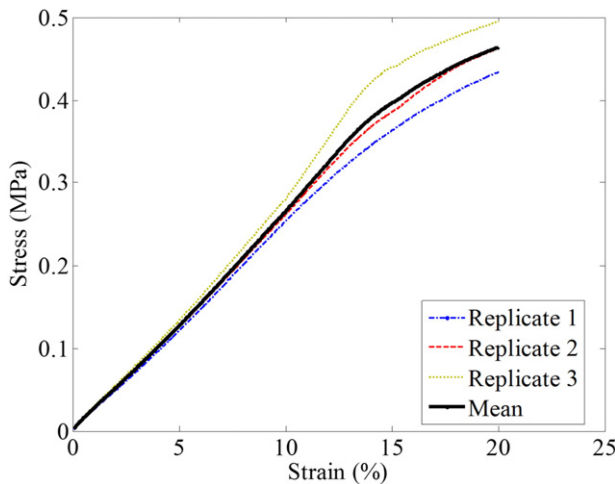


Fig. 5. Stress–strain curves of three replicates and the mean curve of SW_W5A06R03 (default).

Table 3
Specifications of the stress–strain curves of SW_W5A06R03 replicates.

	E_0 (MPa)	$E_{0.2}$ (MPa)	E_t (MPa)	ε_t (%)
Replicate 1	2.34	1.22	2.69	9.1
Replicate 2	2.43	1.16	2.80	9.3
Replicate 3	2.60	0.92	3.74	10.0
Mean (std)	2.46 (0.132)	1.10 (0.159)	3.08 (0.577)	9.5 (0.47)

2.2.2. Variants of the double helix design

The DH design resembles the microstructure of filament actin (F-actin) strands. The default parameter setting of the DH design is $r_H = 0.6$ mm, $h = 5$ mm, and $r_f = 0.2$ mm. Other than the default level, variants with 4 levels of r_H , 4 levels of h , and 2 levels of r_f were designed. Table 2 summarizes a total of 11 variants.

2.3. Materials, equipment, and testing protocols

The meta-material samples were fabricated on a Connex350® 3D printer (Stratasys Ltd). The layer thickness of the printed part is 30 μ m, and the in-plane accuracy is 0.1 mm. The base materials used for the stiff fiber and elastic matrix are VeroBlackPlus® (RGD875) and TangoPlus® (FullCure 930), respectively. These two materials represent the two extremes of printable materials with VeroBlackPlus being the stiffest and TangoPlus the most elastic. The Connex350 can also mix the two base materials at a certain ratio and print them simultaneously to form digital materials that have mechanical properties between the base materials. In the present study, only the base materials were used to prepare the samples. It should be noted that the material choice could also serve as a tuning factor.

Uniaxial tensile tests were conducted using Q800 Dynamic Mechanical Analysis (DMA) (TA Instruments) under a controlled strain mode at room temperature for all samples. The exception was the sample made of pure VeroBlackPlus. These were tested using RSA III DMA (TA Instruments) due to the large Young's modulus. The strain rate was set to a small value of 1%/min to achieve a quasi-static process. The maximum strain was set to 20%. Testing data was analyzed using TA Universal Analysis software and Matlab R2015a.

2.4. Stress–strain curves of the base materials

Although Stratasys provided the basic mechanical properties of VeroBlackPlus and TangoPlus, the elastic moduli are represented by values that varied widely at unknown strain levels. In addition, the

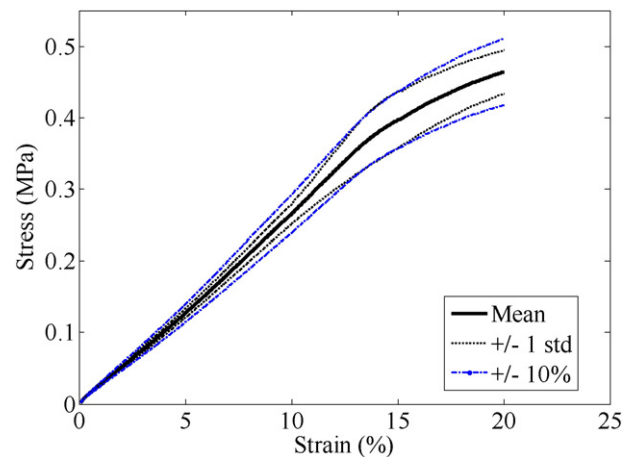


Fig. 6. $\pm 10\%$ mean stress–strain curve and ± 1 standard deviation limits of SW_W5A06R03.

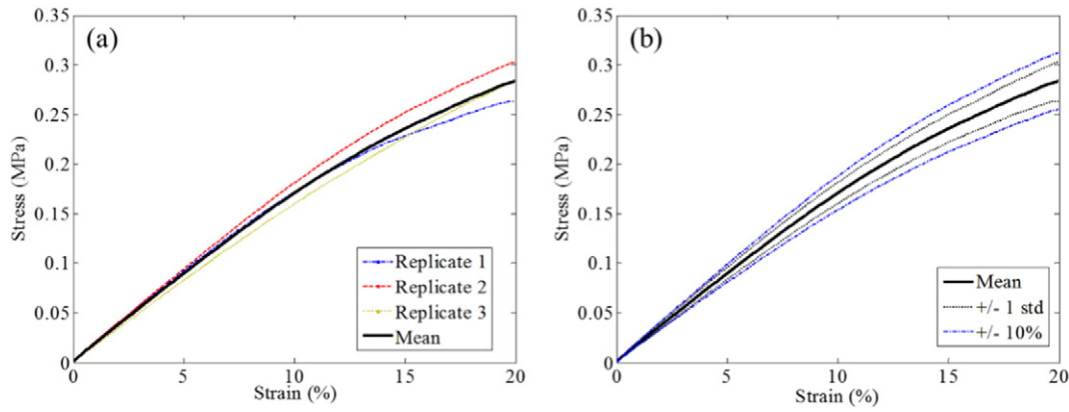


Fig. 7. (a) Stress–strain curves of three replicates and the mean curve of DH_P5H06R02 (default); (b) $\pm 10\%$ mean stress–strain curve and ± 1 standard deviation limits of DH_P5H06R02.

actual properties of the materials in the printed parts are greatly affected by the parameter settings of the printer and how the parts are built. In order to find out the actual mechanical properties of the materials in the samples, we fabricated a pure VeroBlackPlus sample and a pure TangoPlus sample with the same dimension and part orientation as the meta-materials samples. The single-material samples were tested following the same testing protocol described in Section 2.2 and the results are shown in Fig. 4. Both materials exhibited strain-softening as expected.

3. Results and discussions

3.1. Stress–strain curves of the default samples, curve specifications and variations

The results from the uniaxial tensile tests of three replicates of the default SW samples are plotted in Fig. 5. Initially, the three curves were very close to each other, but the discrepancy became larger at higher strain levels. This could be the result of various levels of printing defects existing in those samples.

The three curves and the mean curve show a concavity change. The inflection point, where the curve changes from convex to concave, was mathematically determined by finding the point where the second derivative changes sign. It is obvious that the first derivative of the curve, Young's modulus, achieves its maximum level at the inflection point. The initial modulus (E_0), the modulus at 20% strain ($E_{0.2}$), the maximum modulus (E_i), and the strain at the inflection point (ε_i), were the key specifications used to characterize a stress–strain curve in this study. For the default SW design, the results are listed in Table 3.

Although a larger variation exists among three replicates at higher strain levels, the ± 1 standard deviation limits are still within $\pm 10\%$ of the mean values in the 0–20% strain range, as illustrated in Fig. 6. Considering that 3D printed parts usually have large variations [37,38,39], the repeatability of the stress–strain curve of the SW design is acceptable.

Similarly, the testing results for the default DH design samples are presented in Fig. 7 and Table 4. Compared to the SW default samples, the DH default samples did not have strong convex trends in their stress–strain curves. The inflection points were all at a small strain

level around 2%. At larger strain levels, the curves were mostly concave, indicating a strain-softening behavior.

Like the SW design, the variation among three replicates of the DH default design wasn't large. For the clarity of the plots, the stress–strain curve for each variant is represented by the mean curve with error bars to indicate the standard deviation in the rest of the discussion.

The experimental results of the default samples were compared with theoretical predictions from various composite models, namely the Voigt model, the Reuss model, and a micromechanics model proposed by Shao et al. for composites with wavy fibers [40]. For the dual-material composite sample, the Voigt model gives the upper bound of the Young's modulus. At any given strain ε^* , the Voigt modulus can be calculated as

$$E_{\text{Voigt}}^* = E_1^* V_1 + E_2^* V_2,$$

where E_1^* and E_2^* are the modulus of VeroBlackPlus and TangoPlus at ε^* , respectively. V_1 and V_2 are the volume fraction of VeroBlackPlus and TangoPlus, respectively.

The Reuss model gives the lower bound of the modulus and it can be calculated as.

$$E_{\text{Reuss}}^* = \frac{E_1^* E_2^*}{E_1^* V_2 + E_2^* V_1}.$$

The micromechanics model proposed by Shao et al. in reference [40] replaces the wavy fibers with two types of equivalent straight fibers. Then the effective modulus of the equivalent composite can be calculated using the Mori-Tanaka method. The details of the fiber replacement procedure and the deduction of the equivalency can be found in reference [40].

The results of the comparisons are summarized in Fig. 8. The experimental results indicate that both the SW sample and the DH sample are softer than the prediction given by the micromechanics model. This may be because of the defects in the printed samples and/or the imperfect interface between the fibers and the matrix.

3.2. Effects of parameters for the sinusoidal wave design

3.2.1. Effect of the wavelength

The results of tensile tests for the λ -variants of the SW design are presented in Fig. 9. When other design parameters are fixed, as the wavelength increases, the fiber became more aligned with the direction of the load. As the stiff fibers with a higher degree of alignment carried more load, the initial modulus, E_0 , increased with the wavelength. We noticed that the moduli at 20% strain for all five variants were about the same. The reason is that at this strain level, the fiber structures in the variants were stretched to their limits where the degree of

Table 4
Specifications of the stress–strain curves of DH_P5H06R02 replicates.

	E_0 (MPa)	$E_{0.2}$ (MPa)	E_i (MPa)	ε_i (%)
Replicate 1	1.81	0.71	1.85	1.7
Replicate 2	1.84	0.98	1.87	1.6
Replicate 3	1.64	0.80	1.64	2.0
Mean (std)	1.76 (0.108)	0.83 (0.138)	1.79 (0.127)	1.77 (0.21)

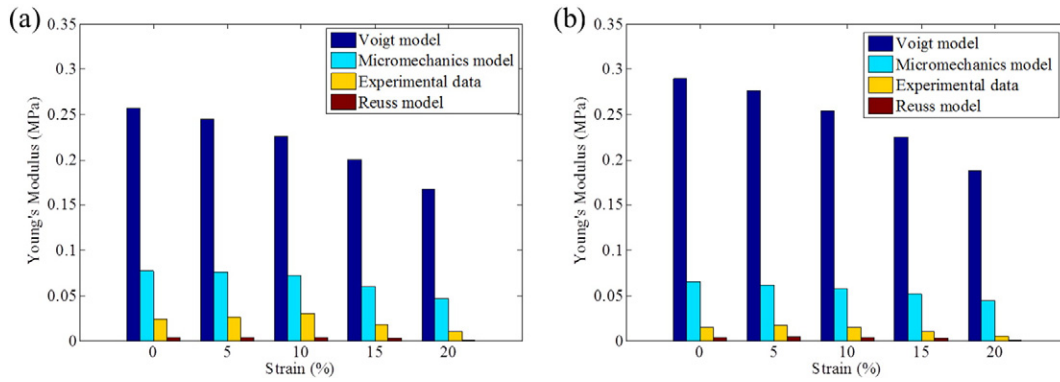


Fig. 8. The comparisons of the predicted Young's moduli and the experimental results at different strain levels: (a) the default SW sample; (b) the default DH sample.

alignment was about 100%. Just like the stretching mechanism of soft tissues discussed in Section 2.1, the mechanical behavior became linear at 5–15% strain, depending on the initial waviness of the fibers. The five variants entered the “linear stage” before 20% strain, therefore they all had similar E_{20} . Obviously, fibers with larger λ/A ratio will reach the straightened state faster. Therefore, variants with a larger wavelength have the inflection points at smaller strain levels. During the tensile test, it was observed that the samples were distorted after the fibers were straightened. This is because the stiff fibers had to push the soft material aside to become straight. The degree of distortion was positively correlated to the deformation of the fibers from their initial state to the straightened state. Hence, the larger E_i of meta-materials with larger fiber wavelength can be explained by the fact that the distortion in those samples was smaller.

3.2.2. Effect of the amplitude

The results of the tensile tests for the A -variants of the SW design are presented in Fig. 10. With the wavelength fixed, changing the amplitude allowed us to investigate the other portion of the λ/A spectrum. Similar to the λ -variants, higher initial modulus and higher maximum modulus were observed in variants with larger λ/A ratio, i.e., smaller A . The location of the inflection point also followed the same trend. When the λ/A is very large (>20), the fibers are almost straight at the initial state. No strain-stiffening effect was seen since the fibers carried most of the load from the beginning of the tensile tests. Also, the variants with straight or near straight fibers, SW_W5A00R03 and SW_W5A02R03, yielded around 4–5%, which is about the same as the strain of yield for VeroBlackPlus.

3.2.3. Effect of the radius of the fiber

The results of tensile tests for the r_f -variants of the SW design are presented in Fig. 11. Unlike the wavelength and the amplitude, changing the radius of fiber did not change the λ/A ratio. It changed the volume fraction of fiber. As expected, increasing values for the initial modulus, maximum modulus, and the modulus at 20% strain were observed as the radius of fiber increased. The existence of a “working window” for the radius of the fiber was also noticed. We observed that if r_f is too small or too large, the soft TangoPlus or the stiff VeroBlackPlus dominated the mechanical behavior of the meta-material. In either case, the meta-material did not give the desired strainstiffening. In this design, the lower limit of this window was between 0.1 mm and 0.2 mm; the upper limit was between 0.3 mm and 0.4 mm.

3.3. Effects of parameters for the double helix design

3.3.1. Effect of the pitch

The results of the tensile tests for the h -variants of the DH design are presented in Fig. 12. A helix can be viewed as a rotating sinusoidal curve in 3D space, where the pitch is like a wavelength in a 2D case. Therefore, the effect of pitch is similar to the effect of wavelength. The strain-stiffening feature was much weaker in the DH h -variants, as observed in the default DH samples. The change of convexity happened at very low strain levels ($<2\%$) for all variants.

3.3.2. Effect of the radius of the helix

The results of tensile tests for the r_H -variants of the DH design are presented in Fig. 13. The radius of the helix had an effect similar to the amplitude in the SW design. The h/r_H ratio, like the λ/A ratio for the

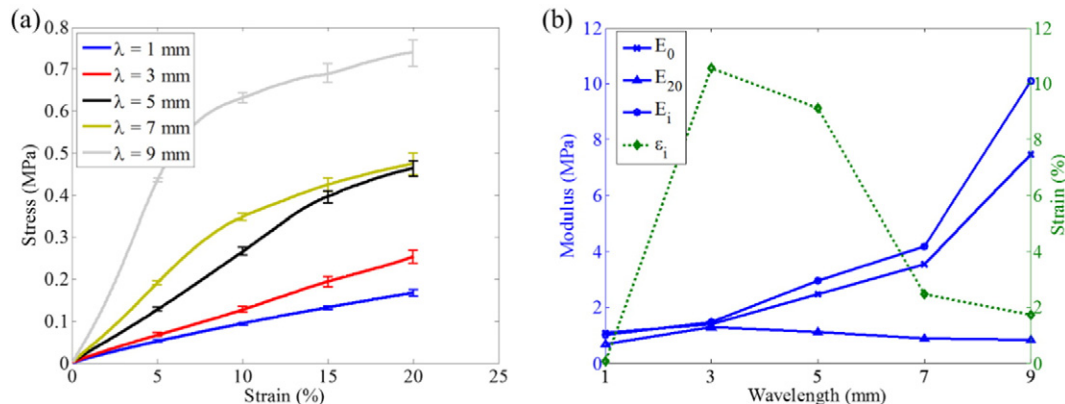


Fig. 9. (a) The stress–strain curves of the SW design with different wavelengths; (b) the effect of the wavelength on curve specifications.

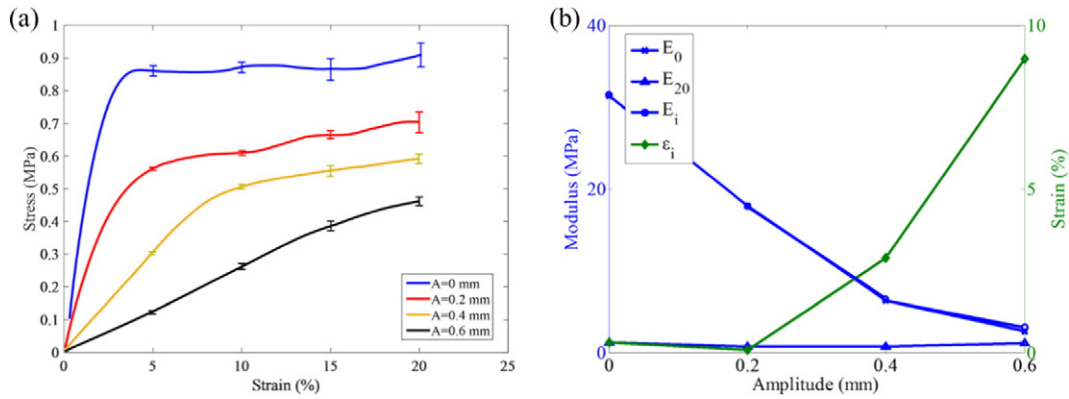


Fig. 10. (a) The stress–strain curves of the SW design with different amplitudes; (b) the effect of the amplitude on curve specifications.

SW design, was used to tune the location of the inflection point. In general, E_0 and E_i were positively correlated to the h/r_f ratio while ϵ_i was negatively correlated.

3.3.3. Effect of the radius of the fiber

The results of tensile tests for the r_f -variants of the DH design are presented in Fig. 14. As expected, all three moduli increased as the radius of the fiber increased. A clear strain-stiffening behavior was observed on samples where the fiber had a larger radius, while the samples with thinner fibers had no such feature.

3.4. Case study: patient-specific aortic valve phantoms for pre-transcatheter aortic valve replacement (TAVR) assessment

Aortic stenosis (AS) is the most common and severe valvular heart disease that affects about 12% of the population aged 75 years or older [41], among whom more than 25% will eventually develop severe AS and need valvular replacement. While historically surgery is the standard treatment, it is not suitable for many of the patients who are at high surgical risk because of advanced age or comorbidities. TAVR has recently been introduced as an alternative treatment option for severe AS patients who are at high surgical risk [42,43]. The procedural success of TAVR predominately relies on pre-TAVR assessment. One of the important gaps in the assessment is the inability to select the prosthesis for a specific patient based on its effects on aortic root mechanics and flow dynamics. Currently, the assessment can only be done using complex computational simulation using a number of assumptions. 3D printing has been proposed as a fast and cost-effective way to accurately reproduce the patient-specific aortic root anatomy for education or training purposes [44,45]. Compared to numerical models, the 3D

printed phantoms provide a more realistic hands-on experience for the physicians performing procedures. However, such phantoms are not suitable for physiological assessment because their material properties are vastly different from the biological aortic tissues.

In this case study, we approximated the stress–strain curve of a typical aortic tissue with the dual-material 3D printed meta-material. An SW design with $\lambda = 0.8$ mm, $A = 0.65$ mm, and $r_f = 0.1$ mm was adopted for the meta-material sample. The comparison of the real aortic tissue, a pure TangoPlus sample, and the meta-material sample is shown in Fig. 15. Although the mechanical properties of the meta-material is still different than real tissue, the stress–strain curve of the meta-material followed the trend better than the pure TangoPlus sample did because the fibers straightened in the meta-materials, which compensated for the creep of the matrix. The dual-material 3D printing provided a way to tweak the mechanical behavior of the printed meta-materials. Nevertheless, great efforts need to be made to expand the design space so that the mechanical behavior of real aortic tissues can be achieved.

4. Conclusions

In this study, two types of dual-material 3D printed meta-materials were designed to mimic the strain-stiffening behavior of soft tissues. The effects of design parameters, i.e. wavelength, amplitude, and radius of fiber for the SW design, pitch, radius of helix, and radius of fiber for the DH design, were investigated by sensitivity analysis. The results from tensile tests indicated that the mechanical behavior of dual-materials meta-materials could be tuned by changing the design parameters. Although the correlation between the specifications of the stress–strain curve and the design parameters is nonlinear and demands

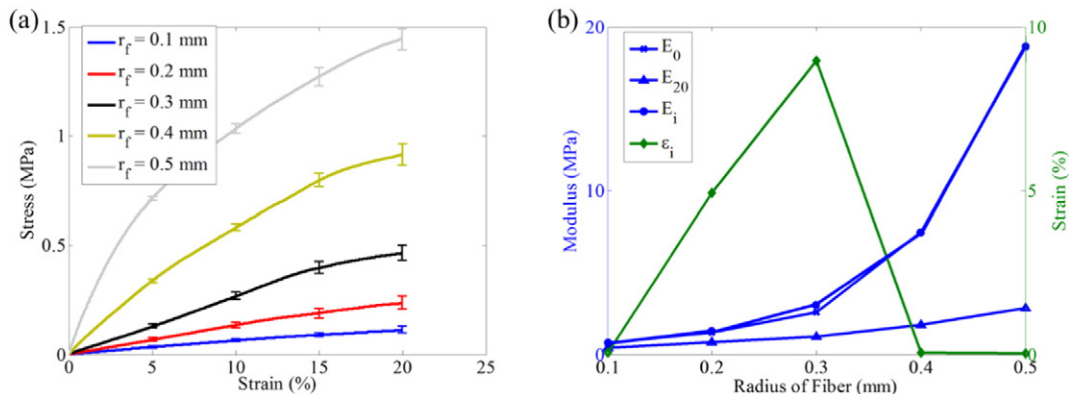


Fig. 11. (a) The stress–strain curves of the SW design with different radii of the fiber; (b) the effect of the radius of the fiber on curve specifications.

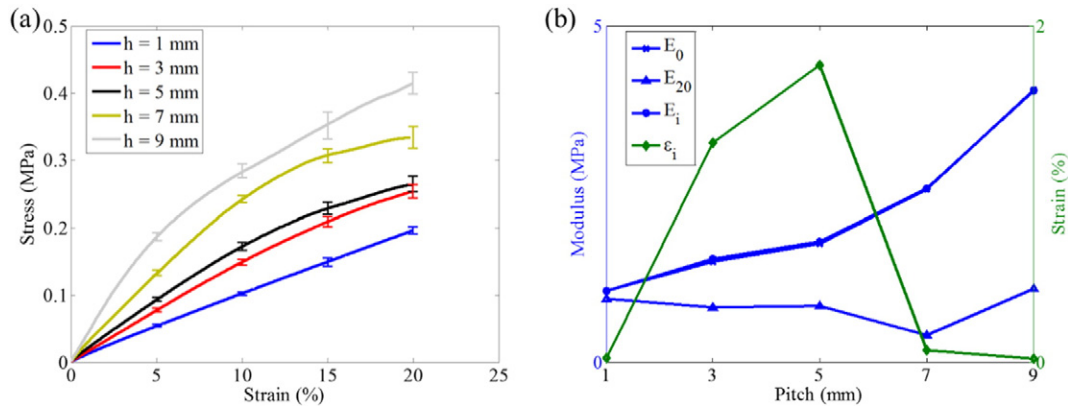


Fig. 12. (a) The stress–strain curves of the DH design with different pitches; (b) the effect of the pitch on curve specifications.

further investigation, there are a few general design guidelines observed during the experiments that are summarized below:

- 1) The volume fraction of stiff fibers needs to be in a moderate range to prevent the mechanical behavior from being dominated by either material;
- 2) The “aspect ratio” a , i.e., λ/A for the SW design and h/r_H for the DH design, can potentially be a good indicator for the strain-stiffening effect. E_0 and E_i are positively correlated to a , and ϵ_i is negatively correlated to a ;
- 3) The radius of the fiber, r_f , can be used as a tuning parameter for the overall stiffness of the meta-material.

Although the design space is currently limited by the material options and 3D printing technologies, this dual-material meta-material design provides a potential method to bridge the inherent difference in mechanical behaviors of soft tissues and polymers. On the other hand, the strain-stiffening effects exhibited in the proposed designs were much weaker than what human tissues have. Great efforts need to be made to simulate real tissue with 3D printed phantoms. With evolving additive manufacturing technologies, it will be possible to fabricate “plastic tissues” with accurate mechanical properties that are associated with gender, age, ethnicity, and other physiological/pathological characteristics of a patient. Being able to represent the bio-mechanical responses, the mechanically accurate, patient-specific,

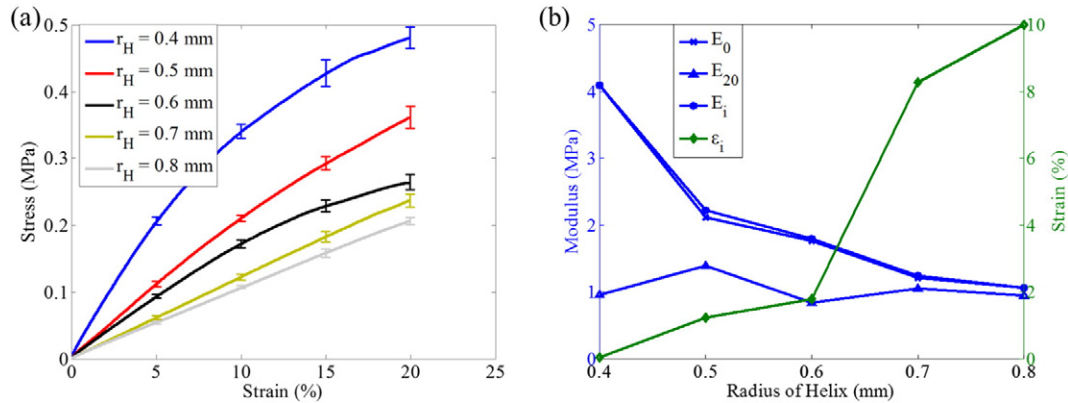


Fig. 13. (a) The stress–strain curves of the DH design with different radii of the helix; (b) the effect of the radius of the helix on curve specifications.

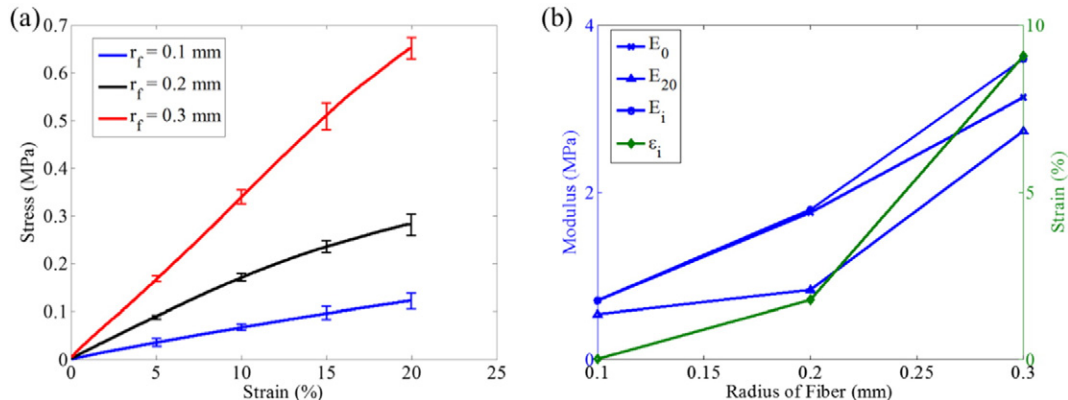


Fig. 14. (a) The stress–strain curves of the DH design with different radii of the fiber; (b) the effect of the radius of the fiber on curve specifications.

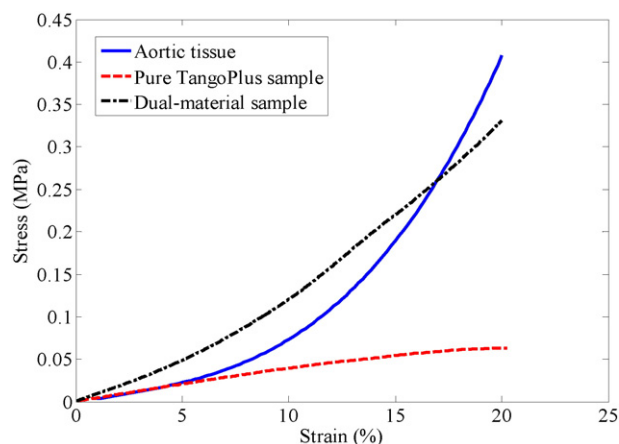


Fig. 15. The comparison of stress–strain curves of a typical aortic tissue, a pure TangoPlus sample, and a dual-material sample. The dual-material sample used the SW design with $\lambda = 0.8$ mm, $A = 0.65$ mm and $r_f = 0.1$ mm.

tissue-mimicking phantoms would find more applications than the current geometry-only phantoms. In addition, this materials design and manufacturing methodology can also be used to fabricate materials and structures for other broader applications beyond biomedical areas where customized structures with tailorable properties are needed.

References

- [1] E.L. Madsen, J.A. Zagzebski, G.R. Frank, An anthropomorphic ultrasound breast phantom containing intermediate-sized scatterers, *Ultrasound Med. Biol.* 8 (4) (1982) 381–392.
- [2] E.L. Madsen, E. Kelly-Fry, G.R. Frank, Anthropomorphic phantoms for assessing systems used in ultrasound imaging of the compressed breast, *Ultrasound Med. Biol.* 14 (Suppl. 1) (1988) 183–201.
- [3] R.A. Kruger, K.K. Kopecky, A.M. Aisen, D.R. Reinecke, G.A. Kruger, W.L. Kiser Jr., Thermoacoustic CT with radio waves: a medical imaging paradigm 1, *Radiology* 211 (1) (1999) 275–278.
- [4] J.C. Blechinger, E.L. Madsen, G.R. Frank, Tissue-mimicking gelatin-agar gels for use in magnetic resonance imaging phantoms, *Med. Phys.* 15 (4) (1988) 629–636.
- [5] E.L. Madsen, G.D. Fullerton, Prospective tissue-mimicking materials for use in NMR imaging phantoms, *Magn. Reson. Imaging* 1 (3) (1982) 135–141.
- [6] P.M. Fong, D.C. Keil, M.D. Does, J.C. Gore, Polymer gels for magnetic resonance imaging of radiation dose distributions at normal room atmosphere, *Phys. Med. Biol.* 46 (12) (2001) 3105–3113.
- [7] K.J. Surry, H.J. Austin, A. Fenster, T.M. Peters, Poly(vinyl alcohol) cryogel phantoms for use in ultrasound and MR imaging, *Phys. Med. Biol.* 49 (24) (2004) 5529–5546.
- [8] W.D. D'Souza, E.L. Madsen, O. Unal, K.K. Vigen, G.R. Frank, B.R. Thomadsen, Tissue mimicking materials for a multi-imaging modality prostate phantom, *Med. Phys.* 28 (4) (2001) 688–700.
- [9] M. Lazebnik, E.L. Madsen, G.R. Frank, S.C. Hagness, Tissue-mimicking phantom materials for narrowband and ultrawideband microwave applications, *Phys. Med. Biol.* 50 (18) (2005) 4245–4258.
- [10] R.K. Wang, Z. Ma, S.J. Kirkpatrick, Tissue Doppler optical coherence elastography for real time strain rate and strain mapping of soft tissue, *Appl. Phys. Lett.* 89 (14) (2006) 144103.
- [11] M.-K. Sun, J. Shieh, C.-W. Lo, C.-S. Chen, B.-T. Chen, C.-W. Huang, W.-S. Chen, Reusable tissue-mimicking hydrogel phantoms for focused ultrasound ablation, *Ultrason. Sonochem.* 23 (2015) 399–405.
- [12] O. Lund, V. Chandrasekaran, R. Grocott-Mason, H. Elwidai, R. Mazhar, A. Khaghani, A. Mitchell, C. Ilsley, M.H. Yacoub, Primary aortic valve replacement with allografts over twenty-five years: valve-related and procedure-related determinants of outcome, *J. Thorac. Cardiovasc. Surg.* 117 (1) (1999) 77–91.
- [13] J.M. Brown, S.M. O'Brien, C. Wu, J.A.H. Sikora, B.P. Griffith, J.S. Gammie, Isolated aortic valve replacement in North America comprising 108,687 patients in 10 years: changes in risks, valve types, and outcomes in the society of thoracic surgeons national database, *J. Thorac. Cardiovasc. Surg.* 137 (1) (2009) 82–90.
- [14] A. Tsamis, J.T. Krawiec, D.A. Vorp, Elastin and collagen fibre microstructure of the human aorta in ageing and disease: a review, *J. R. Soc. Interface* (2013) 10(83).
- [15] A.J. Cloonan, D. Shahmirzadi, R.X. Li, B.J. Doyle, E.E. Konofagou, T.M. McGloughlin, 3D-printed tissue-mimicking phantoms for medical imaging and computational validation applications, *3D Printing Addit. Manuf.* 1 (1) (2014) 14–23.
- [16] A. Sulaiman, L. Boussel, F. Tacconet, J.M. Serfaty, H. Alsaïd, C. Attia, L. Huet, P. Douek, In vitro non-rigid life-size model of aortic arch aneurysm for endovascular prosthesis assessment, *Eur. J. Cardiothorac. Surg.* 33 (1) (2008) 53–57.
- [17] D.W. Hutmacher, Scaffolds in tissue engineering bone and cartilage, *Biomaterials* 21 (24) (2000) 2529–2543.
- [18] A. Curodeau, E. Sachs, S. Caldarise, Design and fabrication of cast orthopedic implants with freeform surface textures from 3-D printed ceramic shell, *J. Biomed. Mater. Res.* 53 (5) (2000) 525–535.
- [19] D.W. Hutmacher, M. Sittlinger, M.V. Risbud, Scaffold-based tissue engineering: rationale for computer-aided design and solid free-form fabrication systems, *Trends Biotechnol.* 22 (7) (2004) 354–362.
- [20] F.P.W. Melchels, M.A.N. Domingos, T.J. Klein, J. Malda, P.J. Bartolo, D.W. Hutmacher, Additive manufacturing of tissues and organs, *Prog. Polym. Sci.* 37 (8) (2012) 1079–1104.
- [21] D. Seliktar, D. Dikovskiy, E. Napadensky, Bioprinting and tissue engineering: recent advances and future perspectives, *Isr. J. Chem.* 53 (9–10) (2013) 795–804.
- [22] S.V. Murphy, A. Atala, 3D bioprinting of tissues and organs, *Nat. Biotechnol.* 32 (8) (2014) 773–785.
- [23] E.J. Weinberg, M.R.K. Mofrad, Transient, three-dimensional, multiscale simulations of the human aortic valve, *Cardiovasc. Eng.* 7 (4) (2007) 140–155.
- [24] E. Lansac, H.S. Lim, Y. Shomura, K.H. Lim, N.T. Rice, W. Goetz, C. Acar, C.M.G. Duran, A four-dimensional study of the aortic root dynamics, *Eur. J. Cardiothorac. Surg.* 22 (4) (2002) 497–503.
- [25] M.R. Labrosse, K. Lobo, C.J. Beller, Structural analysis of the natural aortic valve in dynamics: from unpressurized to physiologically loaded, *J. Biomech.* 43 (10) (2010) 1916–1922.
- [26] S. Kulp, Z. Qian, M. Vannan, S. Rinehart, D. Metaxas, Patient-specific aortic valve blood flow simulations, *Biomedical Imaging (ISBI), 2014 IEEE 11th International Symposium on*, IEEE, 2014.
- [27] G. Biglino, P. Verschueren, R. Zegels, A.M. Taylor, S. Schievano, Rapid prototyping compliant arterial phantoms for in-vitro studies and device testing, *J. Cardiovasc. Magn. Reson.* 15 (2) (2013) 1–7.
- [28] S. Kalath, P. Tsipouras, F.H. Silver, Non-invasive assessment of aortic mechanical properties, *Ann. Biomed. Eng.* 14 (6) (1986) 513–524.
- [29] C. Martin, T. Pham, W. Sun, Significant differences in the material properties between aged human and porcine aortic tissues, *Eur. J. Cardiothorac. Surg.* 40 (1) (2011) 28–34.
- [30] K. Wang, C. Wu, Z. Qian, C. Zhang, B. Wang, M. Vannan, Dual-Material 3D Printed Metamaterials with Tunable Mechanical Properties for Patient-Specific Tissue-Mimicking Phantoms, 2015 (Submitted manuscript).
- [31] A.A.H.J. Sauren, M.C. Vanhout, A.A. Vansteenhoven, F.E. Veldpaus, J.D. Janssen, The mechanical-properties of porcine aortic-valve tissues, *J. Biomech.* 16 (5) (1983) 327–337.
- [32] C.A.J. Hoeve, P.J. Flory, The elastic properties of elastin, *J. Am. Chem. Soc.* 80 (24) (1958) 6523–6526.
- [33] M. Nimni, R. Harkness, Molecular structures and functions of collagen, *Collagen*, 1 1988, pp. 1–77.
- [34] F.H. Silver, J.W. Freeman, G.P. Seehra, Collagen self-assembly and the development of tendon mechanical properties, *J. Biomech.* 36 (10) (2003) 1529–1553.
- [35] G.A. Holzapfel, Biomechanics of soft tissue, *The handbook of materials behavior models*, 3 2001, pp. 1049–1063.
- [36] J. Price, P. Piatucci, Y. Fung, Biomechanics. Mechanical Properties of Living Tissues, Springer Verlag, New York, 1981.
- [37] M.W. Barclift, C.B. Williams, Examining variability in the mechanical properties of parts manufactured via polyjet direct 3D printing, *International Solid Freeform Fabrication Symposium*, August, 2012.
- [38] G. Kim, Y. Oh, A benchmark study on rapid prototyping processes and machines: quantitative comparisons of mechanical properties, accuracy, roughness, speed, and material cost, *Proc. Inst. Mech. Eng. B J. Eng. Manuf.* 222 (2) (2008) 201–215.
- [39] A. Pilipovic, P. Raos, M. Serce, Experimental analysis of properties of materials for rapid prototyping, *Int. J. Adv. Manuf. Technol.* 40 (1–2) (2009) 105–115.
- [40] L.H. Shao, R.Y. Luo, S.L. Bai, J. Wang, Prediction of effective moduli of carbon nanotube-reinforced composites with waviness and debonding, *Compos. Struct.* 87 (3) (2009) 274–281.
- [41] R.L.J. Osnabrugge, D. Mylotte, S.J. Head, N.M. Van Mieghem, V.T. Nkomo, C.M. LeReun, A.J.C. Bogers, N. Piazza, A.P. Kappetein, Aortic stenosis in the elderly disease prevalence and number of candidates for transcatheter aortic valve replacement: a meta-analysis and modeling study, *J. Am. Coll. Cardiol.* 62 (11) (2013) 1002–1012.
- [42] D.H. Adams, J.J. Popma, M.J. Reardon, S.J. Yakubov, J.S. Coselli, G.M. Deeb, T.G. Gleason, M. Buchbinder, J. Hermiller, N.S. Kleiman, S. Chetcuti, J. Heiser, W. Merhi, G. Zorn, P. Tadros, N. Robinson, G. Petrossian, G.C. Hughes, J.K. Harrison, J. Conte, B. Maini, M. Mumtaz, S. Chenoweth, J.K. Oh, U.C.C. Investigator, Transcatheter aortic-valve replacement with a self-expanding prosthesis, *N. Engl. J. Med.* 370 (19) (2014) 1790–1798.
- [43] S.K. Kodali, M.R. Williams, C.R. Smith, L.G. Svensson, J.G. Webb, R.R. Makkar, G.P. Fontana, T.M. Dewey, V.H. Thourani, A.D. Pichard, M. Fischbein, W.Y. Szeto, S. Lim, K.L. Greason, P.S. Teirstein, S.C. Malaisrie, P.S. Douglas, R.T. Hahn, B. Whisenant, A. Zajarias, D.L. Wang, J.J. Akin, W.N. Anderson, M.B. Leon, P.T. Investigators, Two-year outcomes after transcatheter or surgical aortic-valve replacement, *N. Engl. J. Med.* 366 (18) (2012) 1686–1695.
- [44] D. Schmauss, C. Schmitz, A.K. Bigdeli, S. Weber, N. Gerber, A. Beiras-Fernandez, F. Schwarz, C. Becker, C. Kupatt, R. Sodian, Three-dimensional printing of models for preoperative planning and simulation of transcatheter valve replacement, *Ann. Thorac. Surg.* 93 (2) (2012) E31–E33.
- [45] D. Schmauss, G. Juchem, S. Weber, N. Gerber, C. Hagl, R. Sodian, Three-dimensional printing for preoperative planning of complex aortic arch surgery, *Ann. Thorac. Surg.* 97 (6) (2014) 2160–2164.